NASA Contractor Report 189177

Direct Coupling Method for Time-Accurate Solution of Incompressible Navier-Stokes Equations

Woo Y. Soh
Sverdrup Technology, Inc.
Lewis Research Center Group
Brook Park, Ohio

May 1992

Prepared for
Lewis Research Center
Under Contract NAS3–25266

National Aeronautics and Space Administration

DIRECT COUPLING METHOD FOR TIME-ACCURATE SOLUTION OF INCOMPRESSIBLE NAVIER-STOKES EQUATIONS

W.Y. Soh
Sverdrup Technology, Inc.
Lewis Research Center Group
Brook Park, Ohio 44142

SUMMARY

A noniterative finite-difference numerical method is presented for the solution of the incompressible Navier-Stokes equations with second-order accuracy in time and space. Explicit treatment of convection and diffusion terms and implicit treatment of the pressure gradient give a single pressure Poisson equation when the discretized momentum and continuity equations are combined. A pressure boundary condition is not needed on solid boundaries in the staggered mesh system. The solution of the pressure Poisson equation is obtained directly by Gaussian elimination. This method is tested on flow problems in a driven cavity and a curved duct.

INTRODUCTION

A finite-difference numerical method is presented in this paper for time-dependent solution of the incompressible Navier-Stokes equations. Owing to the special role of the pressure which results in the absence of a time derivative term of the pressure in the continuity equation, calculation procedures for incompressible flow differ significantly from that for compressible flow. The continuity equation in the form of a constraint prohibits straightforward integration of the system of flow equations with time. To overcome this difficulty Harlow and Welch (ref. 1) have presented the Poisson equation method for pressure by taking a divergence of the momentum equation and combining it with continuity. This has been extended to three space dimensions by Williams (ref. 2).

Chorin (ref. 3) has introduced a fractional step method, which is now more often called the projection method. This scheme has brought forth a variant known as the velocity-pressure method (refs. 4 and 5) and it has become very popular for fluid flow and heat transfer problems in two or three space dimensions. This method generates an intermediate velocity field directly from the momentum equation alone, which does not satisfy the continuity constraint. The intermediate velocity is corrected successively until the new velocity field becomes asymptotically divergence-free. The solution procedure is iterative in nature. Kim and Moin (ref. 6) introduced a pressure-related Poisson equation as a combination of references 1 and 3.

A direct coupling of the momentum and continuity was also proposed by Moin and Kim (ref. 7). This solves the momentum and continuity equations simultaneously to obtain the flow variables, say velocity components and pressure, at the advanced time level. The artificial compressibility method (ref. 8), developed for steady flows, has been modified to yield time-dependent solutions (refs. 9 and 10).

In this paper we present a direct coupling method on a staggered grid, which also calls for the solution of the discrete pressure Poisson equation. Time integration uses an Adams-Bashforth explicit approximation for convection and diffusion terms, and a Crank-Nicolson implicit approximation for the pressure term. The present method is different from the fractional step method since it uses no intermediate variable to be corrected at a later stage.

FORMULATION

The system of equations for incompressible viscous fluid flow can be written in dimensionless form as

$$\frac{\partial \mathbf{u}}{\partial t} + \nabla \cdot (\mathbf{uu}) = -\nabla p + \frac{1}{Re}\nabla^2 \mathbf{u} \tag{1}$$

$$\nabla \cdot \mathbf{u} = 0 \tag{2}$$

where $\mathbf{u}$ is the velocity, p the static pressure, t the time, and Re is the Reynolds number. Equation (1) is the momentum equation in which each velocity component has its own time derivative. In other words, the momentum equation is written in a time evolution form. The continuity equation (2), which is a *constraint* as opposed to an *evolution* equation, should be satisfied at any time.

First, we start with a finite-difference approximation of the time derivatives only. Let us express the finite-difference approximation of the system (eqs. (1) and (2)) as

$$\frac{\mathbf{u}^{n+1} - \mathbf{u}^n}{\Delta t} + \mathbf{C}(\mathbf{u}) - \mathbf{D}(\mathbf{u}) + \mathbf{G}(p) = 0 \tag{3}$$

$$\nabla \cdot \mathbf{u}^{n+1} = 0 \tag{4}$$

where $\mathbf{C}(\mathbf{u})$, $\mathbf{D}(\mathbf{u})$, and $\mathbf{G}(p)$ are the time approximations of the convection, diffusion, and pressure gradient terms, respectively, and the superscript n is the time level. There are various ways to describe these terms in order to maintain second order accuracy in time. If the Crank-Nicolson approximation is used for all terms

$$\mathbf{C}(\mathbf{u}) = \frac{1}{2}\left[\nabla \cdot (\mathbf{uu})^{n+1} + \nabla \cdot (\mathbf{uu})^n\right] \tag{5}$$

$$\mathbf{D}(\mathbf{u}) = \frac{1}{Re}\left(\nabla^2 \mathbf{u}^{n+1} + \nabla^2 \mathbf{u}^n\right) \tag{6}$$

$$\mathbf{G}(p) = \frac{1}{2}\left(\nabla p^{n+1} + \nabla p^n\right) \tag{7}$$

This is a nonlinear simultaneous system of equations, hence, iteration using a block inversion or sequential scalar inversion is required. To avoid the nonlinearity the convective term $\nabla \cdot (\mathbf{uu})^{n+1}$ in $\mathbf{C}(\mathbf{u})$ can be approximated by

$$\nabla \cdot (\mathbf{uu})^{n+1} \equiv \frac{\partial}{\partial x_q}(u_p u_q)^{n+1} = \frac{\partial}{\partial x_q}(u_p u_q)^n + \frac{\partial}{\partial x_q}\left[\frac{\partial}{\partial u_r}(u_p u_q)^n \Delta u_r\right] + O\left(\Delta t^2\right) \tag{8}$$

where $\Delta u_r = u_r^{n+1} - u_r^n$. Cartesian tensor notation is invoked in the above expression, with subscripts p, q, and r taking values 1,2,3, and with the summation convention applying. The system (eqs. (3) and (4)) with the use of equation (8) can be written in component form as

$$\begin{pmatrix} M & \frac{\Delta t}{2}\frac{\partial(u\cdot)}{\partial y} & \frac{\Delta t}{2}\frac{\partial\cdot}{\partial x} \\ \frac{\Delta t}{2}\frac{\partial(v\cdot)}{\partial x} & N & \frac{\Delta t}{2}\frac{\partial\cdot}{\partial y} \\ \frac{\partial\cdot}{\partial x} & \frac{\partial\cdot}{\partial y} & 0 \end{pmatrix}^n \begin{pmatrix} u^{n+1} \\ v^{n+1} \\ p^{n+1} \end{pmatrix} = \begin{pmatrix} u - \frac{\Delta t}{2}\left(\frac{\partial p}{\partial x} - \frac{1}{Re}\nabla^2 u\right) \\ v - \frac{\Delta t}{2}\left(\frac{\partial p}{\partial y} - \frac{1}{Re}\nabla^2 v\right) \\ 0 \end{pmatrix}^n \tag{9}$$

where

$$M = 1 + \frac{\Delta t}{2}\left[\frac{\partial}{\partial x}(2u^n\cdot) + \frac{\partial}{\partial y}(v^n\cdot) - \frac{1}{Re}\left(\frac{\partial^2\cdot}{\partial x^2} + \frac{\partial^2\cdot}{\partial y^2}\right)\right]$$

$$N = 1 + \frac{\Delta t}{2}\left[\frac{\partial}{\partial x}(u^n\cdot) + \frac{\partial}{\partial y}(2v^n\cdot) - \frac{1}{Re}\left(\frac{\partial^2\cdot}{\partial x^2} + \frac{\partial^2\cdot}{\partial y^2}\right)\right]$$

This system requires block matrix inversion at each grid point. Furthermore, the coefficients of the matrix should be calculated at each time step because of the implicit treatment of the convection terms. Consequently, the direct solution procedure must be repeated every time level. If convection is treated explicitly using the Adams-Bashforth approximation, equation (5) becomes

$$\mathbf{C(u)} = \frac{1}{2}\left[3\nabla\cdot(\mathbf{uu})^n - \nabla\cdot(\mathbf{uu})^{n-1}\right] \tag{10}$$

Then, the operators M and N in equation (9) become $\left[1 - \Delta t(2\,Re)^{-1}\nabla^2\right]$. In this case, the matrix coefficients are to be determined once and remain unchanged throughout the entire calculation. However, a simultaneous solution for u, v, and p is needed, which requires a block matrix inversion.

In the approach which will be used in this paper, the diffusion as well as the convection terms are treated explicitly using the Adams-Bashforth method. The diffusion term becomes

$$\mathbf{D(u)} = \frac{1}{2\,Re}\left(3\nabla^2\mathbf{u}^n - \nabla^2\mathbf{u}^{n-1}\right) \tag{11}$$

Then, equation (9) becomes

$$\begin{pmatrix} 1 & 0 & \frac{\Delta t}{2}\frac{\partial \cdot}{\partial x} \\ 0 & 1 & \frac{\Delta t}{2}\frac{\partial \cdot}{\partial y} \\ \frac{\partial \cdot}{\partial x} & \frac{\partial \cdot}{\partial y} & 0 \end{pmatrix} \begin{pmatrix} u^{n+1} \\ v^{n+1} \\ p^{n+1} \end{pmatrix} = \begin{pmatrix} u^n - \frac{\Delta t}{2}\left(\frac{\partial p}{\partial x}\right)^n + \Delta t\left(D_x - C_x\right) \\ v^n - \frac{\Delta t}{2}\left(\frac{\partial p}{\partial y}\right)^n + \Delta t\left(D_y - C_y\right) \\ 0 \end{pmatrix} \tag{12}$$

here, C_α and D_α are α-components of $\mathbf{C}(\mathbf{u})$ and $\mathbf{D}(\mathbf{u})$ described in equations (10) and (11). The operators M and N in this case become the identity operator, so that a simultaneous solution procedure for u, v, and p can be avoided if the momentum equation is combined with the continuity equation in an appropriate manner. The purpose of this paper is to utilize the time approximation in equation (12), with convection and diffusion terms explicitly treated and the pressure implicitly approximated.

For convenience, the space discretization will be described in a two-dimensional Cartesian coordinate system, but it is readily extendable to three-dimensional space. Figure 1 shows the staggered mesh system for the spatial finite-difference formulation. In the staggered grid, the discretization of equation (12) yields

$$\frac{u_{ij}^{n+1} - u_{ij}^{n}}{\Delta t} + \frac{p_{i+1j}^{n+1} - p_{ij}^{n+1}}{2\Delta x} = (Ru)_{ij} \tag{13}$$

$$\frac{v_{ij}^{n+1} - v_{ij}^{n}}{\Delta t} + \frac{p_{ij+1}^{n+1} - p_{ij}^{n+1}}{2\Delta y} = (Rv)_{ij} \tag{14}$$

$$\frac{(u_{ij} - u_{i-1j})^{n+1}}{\Delta x} + \frac{(v_{ij} - v_{ij-1})^{n+1}}{\Delta y} = 0 \tag{15}$$

where

$$(Ru)_{ij} = -\frac{p_{i+1j}^{n} - p_{ij}^{n}}{2\Delta x} - C_x(i,j) + D_x(i,j)$$

$$(Rv)_{ij} = -\frac{p_{ij+1}^{n} - p_{ij}^{n}}{2\Delta y} - C_y(i,j) + D_y(i,j)$$

Details of the central difference formulation for the convection and diffusion terms, which are $C_\alpha(i,j)$ and $D_\alpha(i,j)$, can be found in reference 11. In order to combine the discrete momentum equation with the continuity equation (15), we rewrite equations (13) and (14) at mesh points (i−1,j) and (i,j−1), respectively, to give

$$\frac{u_{i-1j}^{n+1} - u_{i-1j}^{n}}{\Delta t} + \frac{p_{ij}^{n+1} - p_{i-1j}^{n+1}}{2\Delta x} = (Ru)_{i-1j} \qquad (13)'$$

$$\frac{v_{ij-1}^{n+1} - v_{ij-1}^{n}}{\Delta t} + \frac{p_{ij}^{n+1} - p_{ij-1}^{n+1}}{2\Delta y} = (Rv)_{ij-1} \qquad (14)'$$

Substituting u_{ij}^{n+1} and u_{i-1j}^{n+1} from equations (13) and (13)′, and v_{ij}^{n+1} and v_{ij-1}^{n+1} from equations (14) and (14)′ into the continuity equation (15) yields

$$C_w p_{i-1j}^{n+1} + C_e p_{i+1j}^{n+1} + C_c p_{ij}^{n+1} + C_s p_{ij-1}^{n+1} + C_n p_{ij+1}^{n+1} = (Rp)_{ij} \qquad (16)$$

where $C_w = C_e = \Delta x^{-2}$, $C_s = C_n = \Delta y^{-2}$, $C_c = -2(\Delta x^{-2} + \Delta y^{-2})$, and

$$(Rp)_{ij} = (2\Delta t)^{-1}\left[(Ru)_{ij} - (Ru)_{i-1j} + (Rv)_{ij} - (Rv)_{ij-1}\right]$$

The entire system of equations (eqs. (13) to (15)) now reduces to a single scalar equation (16), which is the discrete Poisson equation for pressure. New flow variables at $(n+1)\Delta t$ can be obtained algebraically by putting the pressure solution of equation (16) into equations (13) and (14).

The discrete Poisson equation (eq. (16)) in a five-point stencil form is solved by direct inversion using Gaussian elimination. A pivoting strategy is not needed because the matrix is diagonally dominant. The storage required in this inversion is approximately $2 \times \min(II,JJ) \times \min(II,JJ) \times \max(II,JJ)$, where II,JJ are the number of cells in the x and y directions, respectively. In this formulation the pressure boundary condition is not needed on the boundary such as a wall where the velocity is described. This should not really be a surprise, since pressure is introduced into the incompressible formulation only for the purpose of linking the momentum and continuity equations in their primitive variable form. The pressure boundary condition issue arises when it is needed to solve the *differential* pressure Poisson equation, which is written to be $\nabla^2 p = \partial^2 u_q v_r / \partial x_q \partial x_r$. In the present approach where the momentum and continuity equations are directly combined in their discrete form, the boundary condition is already taken care of by the momentum equation. However, the pressure boundary condition can be obtained by a comparison of the directly coupled system and the *differential* Poisson equation. The boundary condition is equivalent to $\partial p/\partial n = 0$ for an inviscid case and $\partial p/\partial n = Re^{-1}\partial^2 u_n/\partial n^2$ for a viscous case, where n is the are normal variable to the wall. However, the matrix equation (eq. (16)) is singular since all of the discrete equations are not linearly independent. This can be elucidated by looking at continuity in a discrete integral form over cell surfaces. The following expression can be derived by a mass conservation principle,

$$\sum_{\substack{i=1 \\ i \neq \ell}}^{II} \sum_{\substack{j=1 \\ j \neq m}}^{JJ} (\mathbf{u} \cdot \Delta \mathbf{S})_{i,j} = -(\mathbf{u} \cdot \Delta \mathbf{S})_{\ell,m} \qquad (17)$$

where $\Delta \mathbf{S}$ is the area vector with outward normal to the cell surface. The above expression says that any one of the discrete continuity equations can be constructed by adding up all of the continuity difference

equations over the rest of the cells. Therefore, one of the equations should be discarded and the pressure value at the relevent cell can be set arbitrarily. This is a generic feature of incompressible flow calculations, in which the pressure itself is to be adjusted around the arbitrarily fixed value to render the appropriate pressure gradient. The above equation (eq. (17)) is *exact* in our central difference formulation on the staggered grid. Also, equation (17) holds exactly for nonuniform grids and in generalized coordinates if the discrete continuity is written using any conservative scheme. For global mass conservation, in which equation (17) holds exactly, the integral form of the continuity equation is recommended for a stretched grid or for coordinate systems other than Cartesian. This can be done easily by discretizing a surface integral of the mass over an individual cell. In the present work we set $C_w = C_e = C_s = C_n = Rp = 0$ and $C_c = 1$ at (II,JJ) to fix the value p(II,JJ) to be zero.

Because of the explicit treatment of the convection and diffusion terms the method presented here is subject to a stringent numerical stability limitation. This requires use of a time step within the stability limit. We choose the time step to meet the convection and diffusion limits, which have been referred to as Courant and Neumann limits, respectively. The Courant number C_r and Neumann diffusion number D_n are defined as

$$C_r = \Delta t\left(\frac{|u|}{\Delta x} + \frac{|v|}{\Delta x}\right) \quad \text{and} \quad D_n = \frac{\Delta t}{Re}\left(\frac{1}{\Delta x^2} + \frac{1}{\Delta y^2}\right)$$

In the present algorithm using three time levels, the upper limit of D_n is 1/4. However, the value of C_r will be chosen smaller than unity in a heuristic way.

EXAMPLE PROBLEMS

The first example is for unsteady flow inside a square cavity after the upper wall is set in motion impulsively. As a second example, fluid flow in a curved duct of a square cross section is presented. The flow is assumed fully developed, which eliminates downstream variable dependency.

Driven Cavity Flow

Driven cavity flow has been preferrably chosen to test the numerical scheme for incompressible Navier-Stokes equations mainly because of the following two reasons. Firstly, since velocity is clearly described on the flow boundary, no *ad hoc* boundary condition on the velocity is necessary, in contrast to channel flows in which in-and-out flow boundary conditions can be specified in many different ways. Secondly, there is no primary flow direction. Any *a priori* assumption regarding directivity of the flow, which often allows one-dimensional approximation, is not appropriate to apply in this recirculating flow. Therefore, the finite-difference scheme should be more general than the simple upwind differencing method based on one-dimensional analyses. The majority of driven cavity flows have been emphasised for the steady case. Unsteady computations can be found in literatures (refs. 10, 12, and 13) for flows driven by implusively started or oscillatory motion of the lid.

The present example demonstrates flow development with time when the upper lid, $y = 1$, is set in a uniform motion impulsively. Two cases are studied with the Reynolds numbers of 5000 and 10 000, which are reasonably large for incompressible laminar flow calculations. Strict central difference formulation is maintained in both diffusion and convection. No numerical device such as an artificial damping

term or switching of the difference formulation of the convection terms is applied in this study. A 120 by 120 uniform grid is used throughout. For high Reynolds number flow the Courant number limit is more stringent than the Neumann limit. Therefore, only convection stability is considered taking $C_r = 0.6$, in which u and v are set to be unity and zero, respectively. This yields $\Delta t = 0.005$. This value is not an upper limit and the time step could be increased on the same grid without affecting numerical stability.

Bruneau and Jouron (ref. 14) report from their steady calculation that there would be no steady solution for a high Reynolds number flow. They explain that the solution does not converge and if converges, the solution becomes dependent on the grid size for Reynolds numbers larger than 5000. The calculation shows that the appearance and then vanishing of minor vortices repeats in the corner region of the lower part of the cavity during iterations. Goodrich *et al.* (ref. 15) show that the high Reynolds number flow inside the cavity is unsteady in its time asymptotic behavior. To achive this asymtotic oscillatory flow a long term calculation should be performed after an impulsive start. Several thousand nondimensional time units are required in their computation. The objective of the present study is to apply the current numerical method to a physical problem, rather than infer the ultimate oscillatory flow phenomena. Therefore, we focus our attention only on the early development of the impulsively started driven-cavity flow for nondimensional time units of 210 for $Re = 5000$ and 300 for $Re = 10\,000$.

The velocity, length, and time are made dimensionless by the lid velocity U_o, side dimension L, and L/U_o, respectively. The Reynolds number Re is defined to be U_oL/ν, where ν is kinematic viscosity. Immediately after impulsive movement of the lid at uniform velocity $u = 1$, an enormously steep velocity gradient forms in the vicinity of the lid, which gives rise to a huge drag force. The drag coefficient C_d is defined as

$$C_d = \frac{1}{Re}\int_0^1 \left(\frac{\partial u}{\partial y}\right)_{y=1} dx \tag{18}$$

The drag coefficient appears to decrease precipitously to a steady value in a short period of time (this is not shown here but a similar behavior can be found in ref. 10 for $Re = 400$), which easily misleads one to conclude that the flow has reached a steady state. However, it takes a large amount of time to reach the steady state, especially for high Reynolds number flow. The steady state would be stationary, in which no change occurs with time, or oscillatory. Figure 2 shows the velocity profiles of u and v at the geometric centers, $x = 0.5$ and $y = 0.5$, at the end of present calculation. At $t = 210$ for $Re = 5000$ the present results agree very well with the steady solution of Ghia *et al.* (ref. 16). The local maxima of u and v near the bottom and right walls are -0.418 at $y = 0.079$ and -0.536 at $x = 0.954$; whereas theirs are -0.436 at $y = 0.07$ and -0.554 at $x = 0.953$, respectively. The comparison for $Re = 10\,000$ at $t = 300$ in figure 3 shows a quantitative difference. The local maxima of u and v at the geometric centers of the cavity are -0.407 at $y = 0.062$ and -0.501 at $x = 0.963$; whereas theirs are -0.427 at $y = 0.055$ and -0.543 at $x = 0.969$, respectively. This indicates that further time integration is needed to reach the steady solution. As will be shown later, the local flow still changes at $t = 300$, especially in the corner regions.

Figure 4 shows streamfunction contours at six different times for $Re = 5000$. The vortex center is located just underneath the lid immediately after the implusive motion and moves towards the right wall as shown at $t = 1$. Then, the vortex bounces against the wall and heads downward. The contour at $t = 5$ shows the downward movement of the vortex with its outer contour distorted. The distortion of the outer streamlines allows a bulge of attached vortex at the right wall, which is not shown here but it

occurs between $t = 5$ and 10. The vortex, which forms near the middle of the right wall, moves down and resides at the lower right corner as the secondary vortex. As time proceeds the secondary vortices form progressively in the lower-left and upper-left corners. The streamline contours at $t = 100$ and 210 show little difference.

The increments of the streamfuntion contour $\Delta\psi$ are 0.0015 at $t = 1$, 0.004 at 5, and 0.005 at later times. The contours in the corner regions where the secondary vortices reside are made with a different scale since the magnitude of contour level of the secondary vortex is much lower than that of primary vortex. A $\Delta\psi$ of 2×10^{-4} is used at $t = 15$ and 5×10^{-4} afterward. Moffatt eddies (ref. 17) are observed in the lower right corner for times greater than 30. The Moffatt eddies constitute a vortex cascade which consists of a sequence of eddies of decreasing size and rapidly decreasing intensity occurring near a corner between plane boundaries at rest. The innermost vortex at the corner will hereafter be called the tertiary vortex. The tertiary vortex is very small and weak for $Re = 5000$, so no attempt is made to put more contours in it using a finer scale.

At $Re = 10\ 000$ the flow undergoes much more complicated processes. Figure 5 illustrates the time evolution of the flow using streamfunction contours. The early flow development, $t = 1$,3, and 5, is the same as for $Re = 5000$. At $t = 5$ the vortex is seen bulging from the right wall, which later forms the secondary vortex at the lower right corner after $t = 20$. The detatched vortex at $t = 10$ appears relatively strong and it rolls on the bottom wall (not shown), the left wall as shown at $t = 20$, and then finally stays at the upper left corner. This rolling vortex becomes the secondary vortex in the upper corner. At $t = 30$ the contour plot shows that the primary, secondary, and tertiary vortices are well identified at three corners of the cavity. However, the flow is far from steady and even the primary vortex changes its shape and the center long after $t = 30$. This can be seen in all of the contour plots in figure 5. As time procedes further the primary vortex appears to be stabilized qualitatively as shown at $t = 100$ and 300.

As in the case of $Re = 5000$, different scales are used in the streamfunction contour plots of the primary and secondary vortex and no further smaller scale contour is added in the area occupied by tertiary vortex. The tertiary vortices appear in two corners of the lower part, which are much larger in size than that for $Re = 5000$. As shown at times larger than 90 the secondary and tertiary vortices near the lower right corner seem to become stable as time elapses. However, the vortices in the lower left and the upper corner do not tend to be steady. They change incessantly. They may take on oscillatory behavior in the long run.

After a series of spiral motions the primary vortex center finds its ultimate position at (0.5166, 0.5333) for both $Re = 5000$ and 10 000. The present calculation indicates that the primary vortex center does not change in either case after about $t = 120$. This agrees excellently with the result of Ghia *et al.* which shows the vortex centers are (0.5117, 0.5352) and (0.5117, 0.5333) at $Re = 5000$ and 10 000, respectively. The locus of the primary vortex center is shown in figure 6 for $Re = 10\ 000$. (No attempt is made to interpolate adjacent values of streamfunction to yield the exact vortex center. Instead, the maximum streamfuntion value is searched only on the grid point positions.) The vortex center is traced from $t = 0.5$ with a time increments of 0.5.

Fluid Flow in a Curved Duct

Fluid flow in a curved duct has been studied in many engineering applications both for developing and for fully-developed cases. Most of the applications are for the steady flow. Unsteady cases have been

also reported for a pulsatile fluid flow in a curved pipe (refs. 18 and 19), which is relevant to the blood flow through the ascending aorta.

In the present work the flow is at rest initially and it is assumed that a sudden axial pressure gradient is imposed. Also a fully-developed flow assumption is made. This kind of fluid flow could be observed far downstream of a curved duct, whose entrance is connected to a reservior, and an exit valve is opened suddenly. Because of the fully-developed condition postulated the derivatives with respect to the downstream variable φ are to be neglected except the pressure. The cylindrical coordinates (x, y, and φ), along with the corresponding velocity components (u, v, and w), are illustrated in figure 7. The curvature ratio δ is defined to be a/R, where a is the gap, $r_o - r_i$, and R is the radius of curvature. The nondimensional Navier-Stokes equations are given in cylindrical coordinates as

$$\frac{\partial u}{\partial t} + L(u) - \frac{\delta w^2}{B} = -\frac{\partial p}{\partial x} + \frac{1}{R_0}\left(\nabla^2 u - \frac{\delta^2 u}{B^2}\right) \tag{19}$$

$$\frac{\partial v}{\partial t} + L(v) = -\frac{\partial p}{\partial y} + \frac{1}{R_0}\left(\nabla^2 v\right) \tag{20}$$

$$\frac{\partial w}{\partial t} + L(w) + \frac{\delta uw}{B} = \frac{1}{B} + \frac{1}{R_0}\left(\nabla^2 w - \frac{\delta^2 w}{B^2}\right) \tag{21}$$

$$\frac{1}{B}\left[\frac{\partial}{\partial x}(Bu) + \frac{\partial}{\partial y}(Bv)\right] = 0 \tag{22}$$

where $B = 1 + \delta x$ and

$$L(\cdot) = \frac{1}{B}\left[\frac{\partial}{\partial x}(Bu\cdot) + \frac{\partial}{\partial y}(Bv\cdot)\right], \qquad \nabla^2(\cdot) = \frac{1}{B}\left[\frac{\partial}{\partial x}\left(B\frac{\partial \cdot}{\partial x}\right) + \frac{\partial}{\partial y}\left(\frac{\delta^2}{B}\frac{\partial \cdot}{\partial y}\right)\right]$$

The R_0 is the Reynolds number based on a reference velocity W_r because for fully-developed case the mean velocity W_m is only obtained as a part of the solution. The reference velocity has been chosen as

$$W_r = \left(\frac{aG}{\rho}\right)^{1/2} \quad \text{where} \quad G = -\frac{1}{R}\frac{\partial p'}{\partial \varphi}$$

where ρ is the density, p′ the dimensional static pressure, G is the axial pressure gradient which is the driving force maintaining the flow in the duct, and the pressure p is nondimensionalized as $p \,/\left(\rho W_r^2\right)$. The above system of equations is relevent to a rotating fluid flow with an axisymmetric geometry and heat transfer problems because the rotating velocity component and the energy are formally decoupled from the pressure gradient.

In the fully-developed flow case only the cross sectional components of the momentum equation (i.e., u and v equations) are to be combined with the continuity to yield a discrete Poisson equation for the pressure. Due to the area change in the radial direction the continuity is derived to be the surface integral of the mass over the cell rather than using equation (22) directly. This, as mentioned before, exactly satisfies the global mass conservation in a discrete sense. The discrete Poisson equation is constructed as before, using the Adams-Bashforth approximation for the convection and diffusion and Crank-Nicolson for the pressure, as described in section 2. The axial momentum equation (eq. (21)) is integrated using the Peaceman and Rachford type ADI as

$$\frac{w^{n+1/2} - w^n}{\frac{1}{2}\Delta t} + \frac{1}{B}\left[\frac{\partial}{\partial x}\left(Bu^c w^{n+1/2}\right) + \frac{\partial}{\partial y}\left(Bv^c w^n\right)\right] + \frac{\delta u^c w^a}{B} = \frac{1}{B}$$

$$+ \frac{1}{BR_o}\left[\frac{\partial}{\partial x}\left(B\frac{\partial w^{n+1/2}}{\partial x}\right) + \frac{\partial}{\partial y}\left(\frac{\delta^2}{B}\frac{\partial w^n}{\partial y}\right) - \frac{\delta^2 w^a}{B}\right] \tag{23}$$

$$\frac{w^{n+1/2} - w^{n+1/2}}{\frac{1}{2}\Delta t} + \frac{1}{B}\left[\frac{\partial}{\partial x}\left(Bu^c w^{n+1/2}\right) + \frac{\partial}{\partial y}\left(Bv^c w^{n+1}\right)\right] + \frac{\delta u^c w^a}{B} = \frac{1}{B}$$

$$+ \frac{1}{BR_o}\left[\frac{\partial}{\partial x}\left(B\frac{\partial w^{n+1/2}}{\partial x}\right) + \frac{\partial}{\partial y}\left(\frac{\delta^2}{B}\frac{\partial w^{n+1}}{\partial y}\right) - \frac{\delta^2 w^a}{B}\right] \tag{24}$$

where the quantities with the superscripts c and a denote the values at $(n+1/2)\Delta t$ by the Crank-Nicolson and the Adams-Bashforth approximations, respectively. Since u and v at $(n+1)\Delta t$ are already obtained by equations (19) and (20) and the surface integration version of equation (22), it is trivial to obtain these at $(n+1/2)\Delta t$ by the Crank-Nicolson method.

The Reynolds numbers of 120 and 200 are considered with a 60 by 40 grid in the cross plane (x,y). The curvature ratio δ is taken to be 1/6.45. The time step Δt is more restrictive due to the decoupling effect between the w-momentum equation and the pressure (hence the continuity), and is chosen to be 0.0002. Numerical solution is sought over the entire domain of the cross-section, $-0.5 \leq x,y \leq 0.5$. Computations for both $R_o = 120$ and 200 are performed up to $t = 24$, which is considered sufficient for a steady state.

Calculations reveal that the flows for both Reynolds numbers are symmetric about the plane $y = 0$, which will be called the plane of symmetry hereafter. Figure 8 illustrates the main and the secondary flow development for $R_o = 120$. The contour plots are made using only the half domain of the cross-section. The upper half is for the streamfunction and the bottom half is for the w velocity. The cross-flow streamfuntion ψ is defined as

$$u = \frac{\partial \psi}{\partial y} \quad \text{and} \quad v = -\frac{1}{B}\frac{\partial}{\partial x}(B\psi)$$

It is well known that the velocity maximum for steady flow occurs near the outer bend due to a centrifugal effect. Surprisingly, quite the reverse is observed in an early stage of flow evolution, such that the w maximum occurs near the inner bend as shown at $t = 1$ and 2 in figure 8. This maximum migrates towards the outer wall as the flow develops further, which is illustrated at $t \geq 4$. It is observed that the w maximum, which is initially located on the plane of symmetry (shown at $t = 1,2,4$ in the plot), shifts from it and forms double peaks in the entire cross-section. This is shown for $t \geq 8$. The axial flow boundary layer is readily recognized along the outer and bottom (and top) walls. The w distribution near the inner wall is not of boundary layer type because higher velocity fluid particles are squeezed into the outer bend due to the centrifugal force. The contour plots are made with different scales as time changes since the flow variable values are very small in the beginning. The values of Δw are 0.1 at $t = 1$, 0.2 at $t = 2$, and 0.25 at later times.

Immediately after the sudden imposition of the pressure gradient, the secondary flow already takes on a vortex-pair pattern in such a way that fluid particles travel toward the inner bend along the bottom and top walls of the duct, collide and separate at the middle of the inner bend, and reenter through the plane of symmetry toward the outer wall. The strength of the secondary flow is negligible in the very beginning. The streamlines in the top half of the cross-section in figure 8 show the secondary flow history. ($\Delta\psi$ is taken to be 10^{-4} at $t = 1$, 10^{-3} at 2, and 0.005 at $t \geq 4$.) The secondary flow for $R_o = 120$ maintains a single vortex-pair from the beginning with the intensity increasing. It is worth noticing that a minor vortex-pair appears near the outer bend at $t = 14$ and 20. This additional small vortex-pair, which is of Taylor-Görtler type, remains minor at this R_o.

For the case of $R_o = 200$ the flow exhibits more complexity. Figure 9 shows the axial velocity contours over the entire cross-section with $\Delta w = 0.1$ at $t = 2$ and 0.25 at the other times. As in the previous case, the w maximum occurs in the vicinity of the inner bend and gradually shifts toward the outer bend. Migration of the w maximum forms a boundary layer near the outer wall as shown at $t = 6$ and the high velocity contour becomes distorted severely. This can be seen in figure 9 for $t \geq 8$ as an eruption of the wall boundary layer from the middle of the outer wall. This axial flow complexity is closely associated with the secondary flow behavior, which will be seen later in the secondary flow contour plot. The w velocity profiles at $t = 24$ are drawn in figure 10. For $R_o = 120$ the migration of the maximum velocity toward the outer wall can be seen on the plane of symmetry, while the w maximum for $R_o = 200$ is pushed toward the center. Again, the velocity maximum for $R_o = 200$ is seen to shift toward the outer bend and off the plane of symmetry. (y is about 0.14 in fig. 10.)

The secondary flow is complex for $R_o = 200$. The contour plots in the upper half of the cross-section in figure 11 are for the streamfunction. The increment $\Delta\psi$ is taken to be 0.001 at $t = 2$ and 0.005 at $t \geq 4$. One vortex pair, which is maintained in earlier times (shown at $t = 2$ and 4), becomes two vortex-pair. The additional vortex near the outer wall is not minor, but as strong as the primary vortex. The same scale of $\Delta\psi$ is used for both the primary and the additional vortices. The strong vortex near the middle of the outer bend is considered responsible for the appearance of the w maximum near $x = 0$ on the plane of symmetry since it conveys fluid particles away from the outer wall through the symmetry plane.

The v velocity contour is shown in the bottom half of the cross-section. Four extrema (for the full cross-section) in the v velocity correspond to the one-vortex-pair structure in the secondary flow as shown at $t = 2$ and 4. Likewise, eight extrema of the v are seen clearly corresponding to the two-

vortex pair for $t \geq 8$ in figure 11. The Δv is 0.006 at $t = 2$ and 0.03 at $t \geq 4$. The contour of v at $R_o = 120$, which is not shown here, exhibits four large valleys and peaks and additional extrema due to minor vortices at the outer bend are insignificant.

A relation between the reference velocity W_r and the mean velocity W_m can be found as

$$W_m = QW_r \qquad \text{where} \qquad Q = \int_{-1/2}^{+1/2} \int_{-1/2}^{+1/2} w \, dx \, dy$$

The flowrate Q is based on W_r. The Reynolds number defined as $Re = W_m a/\nu$ becomes $Re = QR_o$. The Re is more conveniently used in experiments because the W_m is a direct measure. The same is true in the analysis of spatially developing flow when an inlet velocity profile, hence the Re, is given. Figure 12(a) is for the flowrate Q which is also interpreted as the time history of Re. The values of Q at $t = 24$ are 2.8012 and 3.4645 for $R_o = 120$ and 200, respectively, and the Reynolds numbers become $Re = 336.14$ and 692.9 accordingly. These values are confirmed by the steady solutions by the artificial compressibility method mentioned earlier. Figure 12(b) presents the pressure difference between the outer and the inner wall on the plane of symmetry, which is $\left(p_o' - p_i'\right) / \left(\rho W_r^2\right)$. The dip for $R_o = 200$ appears as a response to the change in the secondary flow structure from one-vortex pair to two-vortex pair. The flowrate history for $R_o = 200$ in figure 12(a) also bears the vestige of the same response.

CONCLUSIONS

With the explicit treatment of the convection and the diffusion and the implicit treatment of the pressure, the direct coupling of the discrete momentum and the continuity equations renders a single pressure equation. Direct inversion of the matrix by the Gaussian elimination provides efficiency and speed of the computation since iteration is not needed each time step. The present method is tested on the driven cavity flow of high Reynolds numbers and the curved duct flow to give second order accurate solutions in time and space. Details of the secondary and tertiary vortices are captured in the driven cavity. The solution for $Re = 5000$ agrees very well with the published data. For $Re = 10\,000$ the result does not show the steady behavior at least within the time units used, but qualitativly agrees with the steady data. It is found that the velocity maximum is located near the inner bend in the early stage of flow development. Time evolution of the main and secondary flow towards the steady state and changes in vortex pattern are clearly simulated.

REFERENCES

1. Harlow, F.H.; and Welch, J.E.: Numerical Calculation of Time-Dependent Viscous Incompressible Flow of Fluid with Free Surface. Phys. Fluids, vol. 8, 1965, pp. 2182-2189.

2. Williams, G.P.: Numerical Integration of the Three-Dimensional Navier-Stokes Equations for Incompressible Flow. J. Fluid Mech., vol. 37, 1969, pp. 727-750.

3. Chorin, A.J.: Numerical Solution of the Navier-Stokes Equations. J. Math. Comput., vol. 22, 1968, pp. 745-762.

4. Hirt, C.W.; and Cook, J.L.: Calculating Three-Dimensional Flows Around Structures and Over Rough Terrain. J. Comput. Phys., vol. 10, no. 2, 1972, pp. 324-340.

5. Peyret, R.: Unsteady Evolution of a Horizontal Jet in a Stratified Fluid. J. Fluid Mech., vol. 78, 1976, pp. 49-63.

6. Kim, J.; and Moin, P.: Application of Fractional-Step Method to Incompressible Navier-Stokes Equations. J. Comput. Phys., vol. 59, 1985, pp. 308-323.

7. Moin, P.; and Kim, J.: On the Numerical Solution of Time-Dependent Viscous Incompressible Fluid Flows Involving Solid Boundaries, J. Comput. Phys., vol. 35, 1980, pp. 381-392.

8. Chorin, A.J.: A Numerical Method for Solving Incompressible Viscous Flow Problems. J. Comput. Phys., vol. 2, 1967, pp. 12-26.

9. Merkle, C.L.; and Athavale, M.: Time-Accurate Unsteady Incompressible Flow Algorithms Based on Artificial Compressibility. AIAA Paper 87-1137, 1987.

10. Soh, W.Y.; and Goodrich, J.W.: Unsteady Solution of Incompressible Navier-Stokes Equations. J. Comput. Phys., vol. 79, 1988, pp. 113-134.

11. Soh, W.Y.: Time-Marching Solution of Incompressible Navier-Stokes Equations for Internal Flow. J. Comput. Phys., vol. 70, 1987, pp. 232-252.

12. Gustafson, K.; and Halasi, K.: Vortex Dynamics of Cavity Flows. J. Comput. Phys., vol. 64, 1986, pp. 279-319.

13. Goodrich, J.W.; and Soh, W.Y.: Time-Dependent Viscous Incompressible Navier-Stokes Equation: The Finite Difference Galerkin Formulation and Streamfunction Algorithms. J. Comput. Phys., vol. 84, 1989, pp. 207-241.

14. Bruneau, C.-H.; and Jouron, C.: An Efficient Scheme for Solving Steady Incompressible Navier-Stokes Equations. J. Comput. Phys., vol. 89, 1990, pp. 389-413.

15. Goodrich, J.W.; Gustafson, K.; and Halasi, K.: Hopf Bifurcation in the Driven Cavity. J. Comput. Phys., vol. 90, 1990, pp. 219-261.

16. Ghia,U.; Ghia, K.N.; and Shin, C.T.: High-Re Solution for Incompressible Flow Using the Navier-Stokes Equations and a Multigrid Method. J. Comput. Phys., vol. 48, 1982, pp. 387-411.

17. Moffatt, H.K.: Viscous and Resistive Eddies Near a Sharp Corner. J. Fluid Mech., vol. 18, 1964, pp. 1-18.

18. Hamakiotes, C.C.; and Berger, S.A.: Fully Developed Pulsatile Flow in a Curved Tube. J. Fluid Mech., vol. 195, 1988, pp. 23-55.

19. Chang, L.-J.; and Tarbell, J.M.: Numerical Simulation of Fully Developed Sinusoidal and Pulsatile (Physiological) Flow in Curved Tubes. J. Fluid Mech., vol. 161, 1985, pp. 175-198.

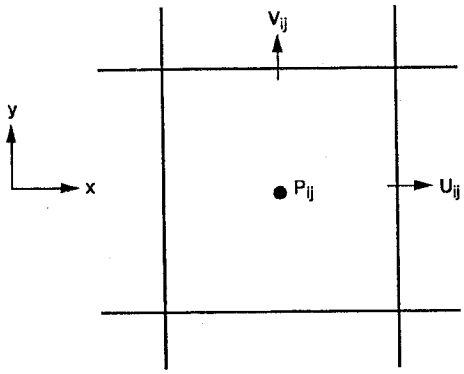

Figure 1.—Staggered grid.

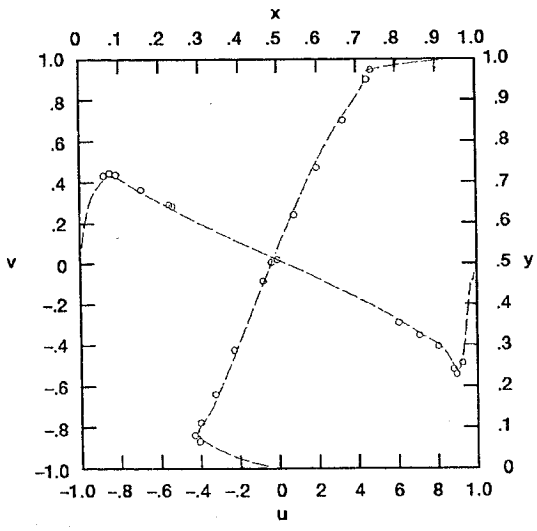

Figure 2.—u and v velocities on the geometric center of the cavity for Re = 5000.

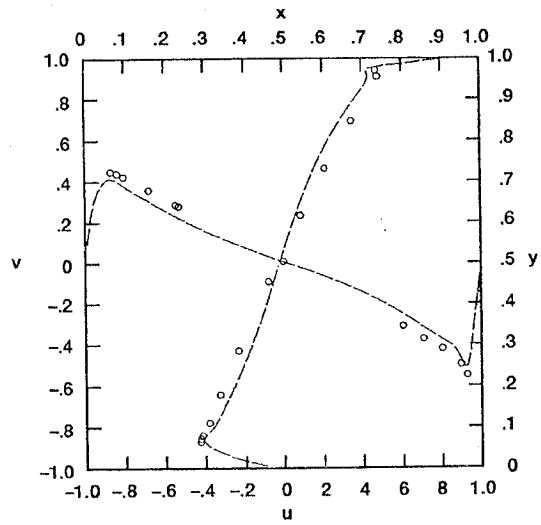

Figure 3.—u and v velocities on the geometric center of the cavity for Re = 10 000.

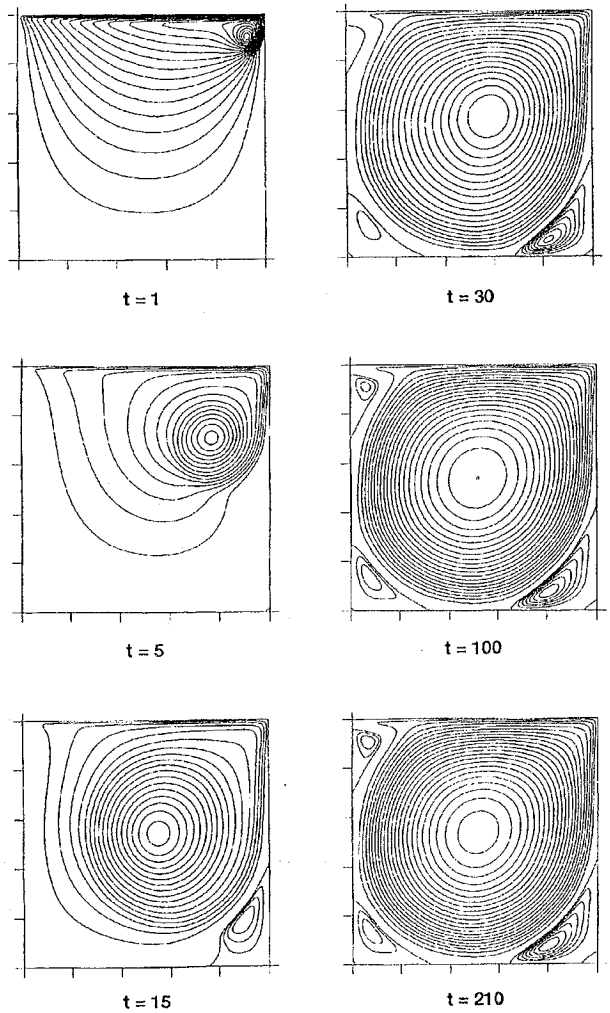

Figure 4.—Streamfunction contours versus time at Re = 5000.

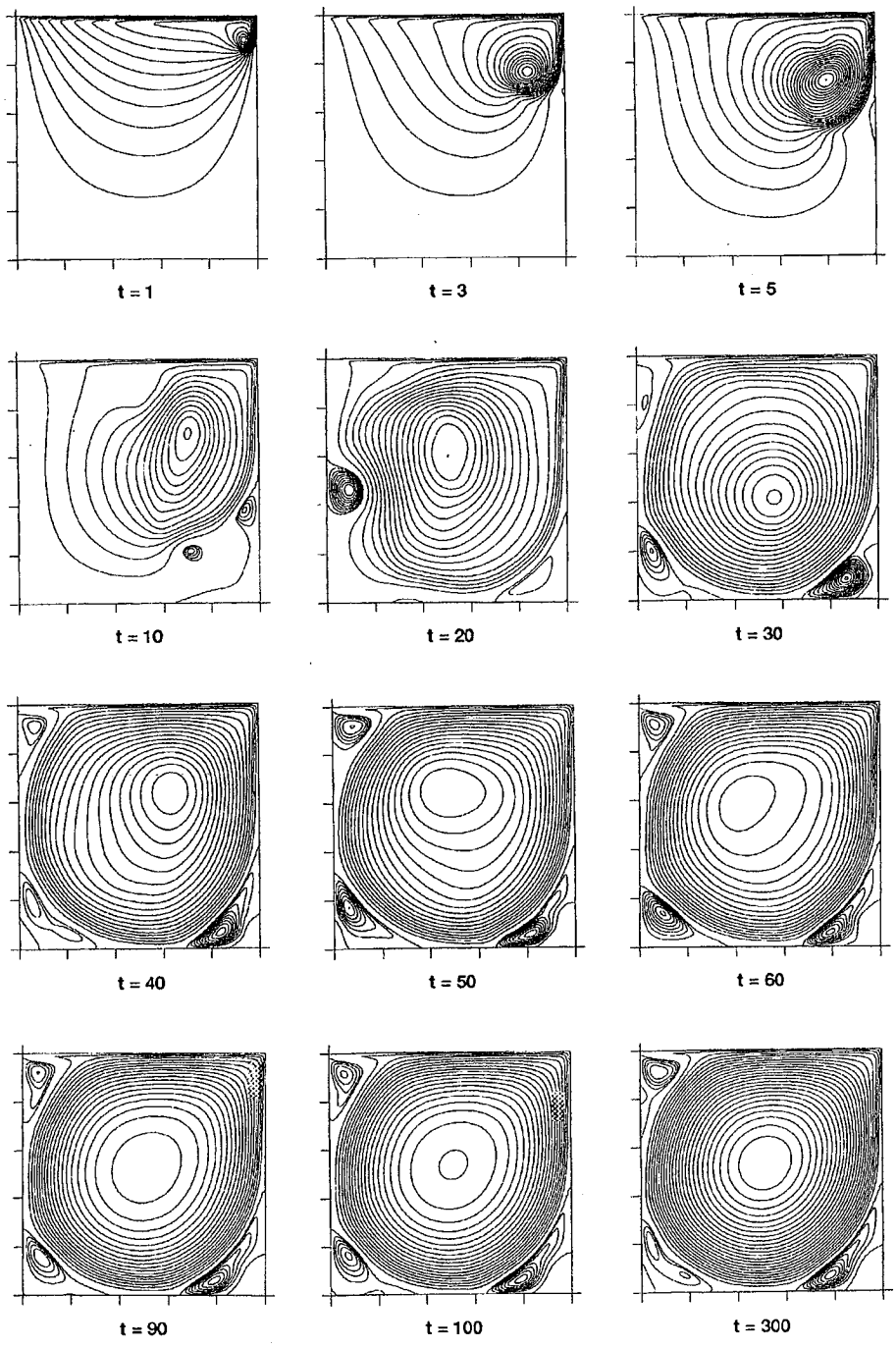

Figure 5.—Streamfunction contours versus time at Re = 10 000.

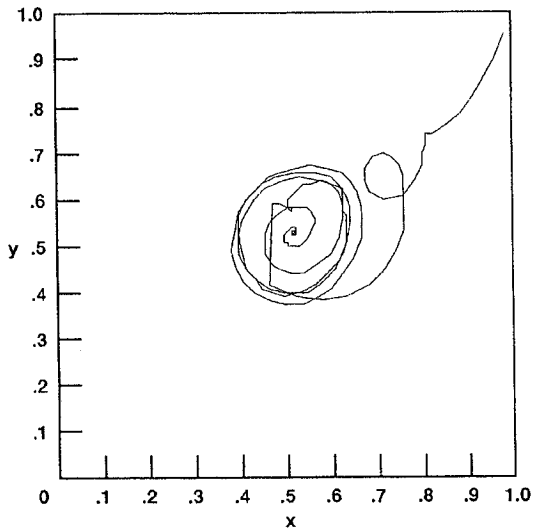

Figure 6.—Locus of the primary vortex center at Re = 10 000.

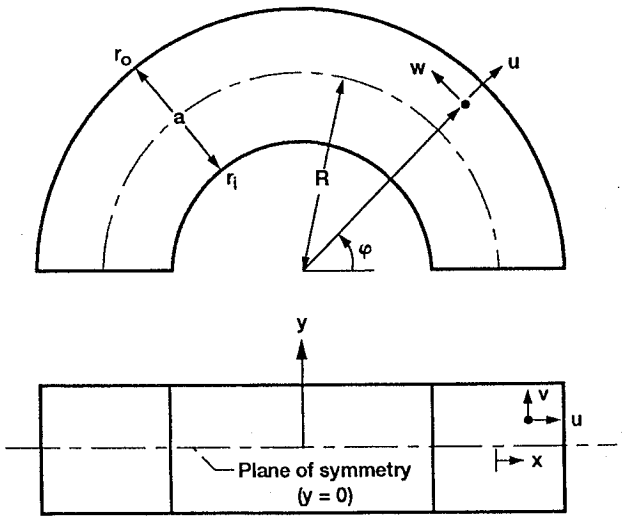

Figure 7.—Cylindrical coordinates and velocity components.

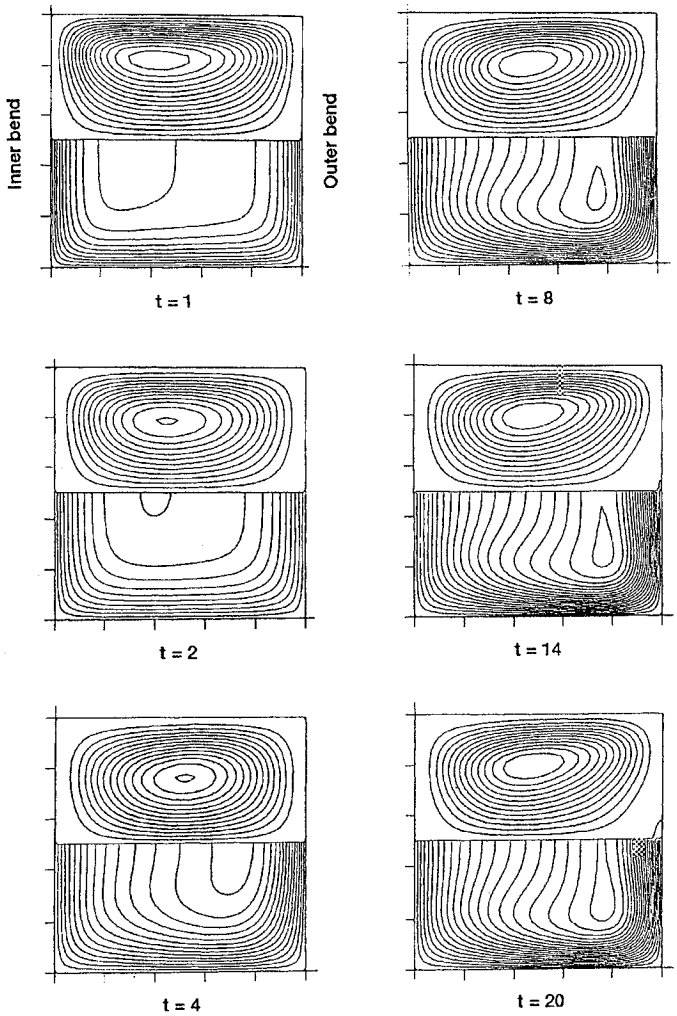

Figure 8.—Axial (main) and secondary flow development for R_o = 120.

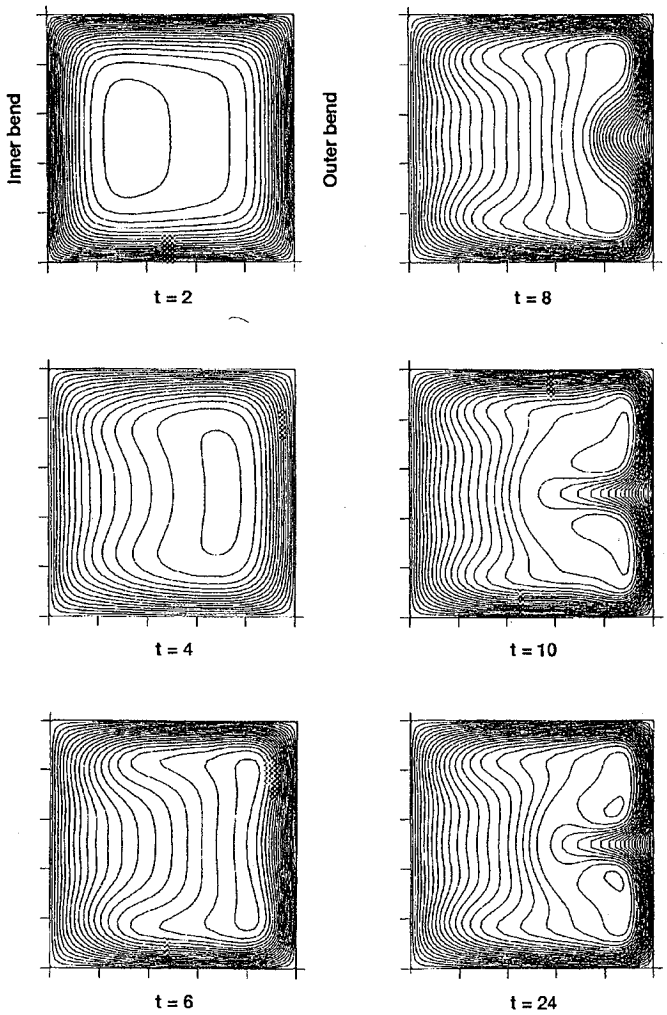

Figure 9.—Axial (main) flow development for $R_o = 200$.

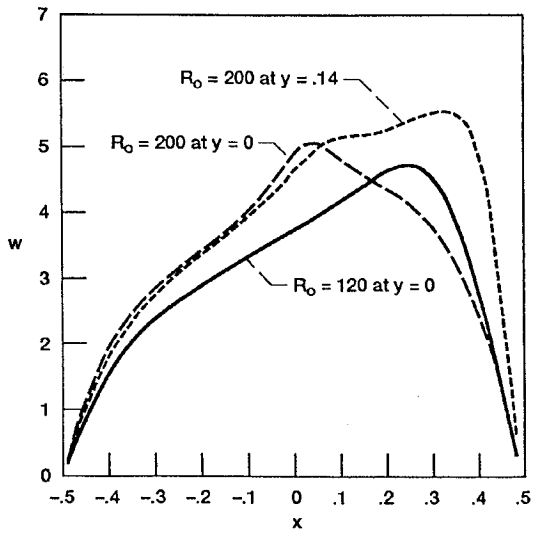

Figure 10.—w-profiles at t = 24.

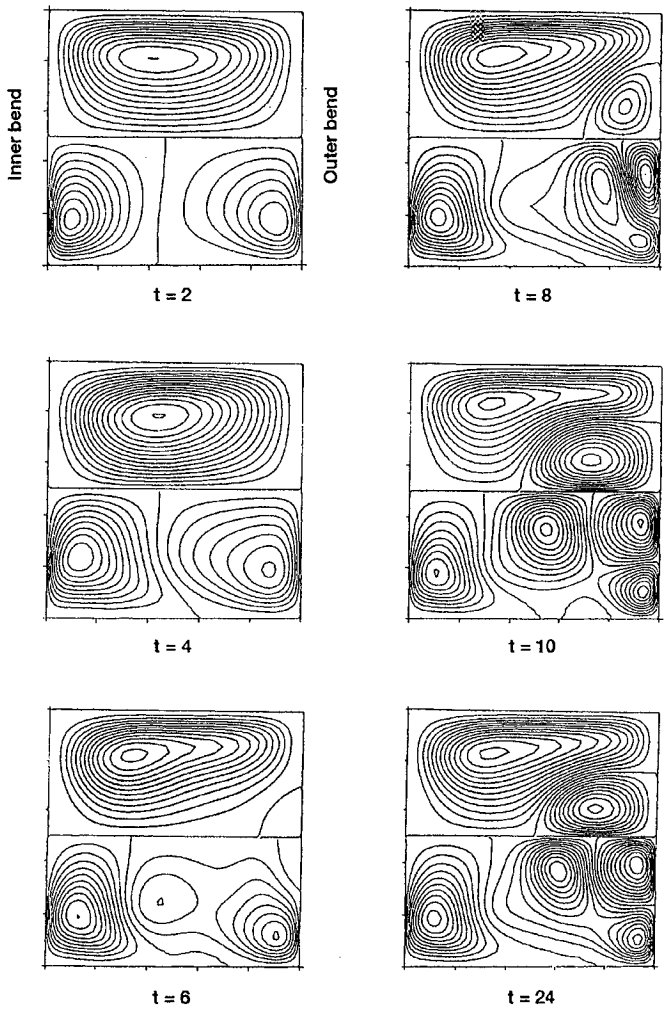

Figure 11.—Secondary flow streamfunction and v-velocity contours for $R_o = 200$.

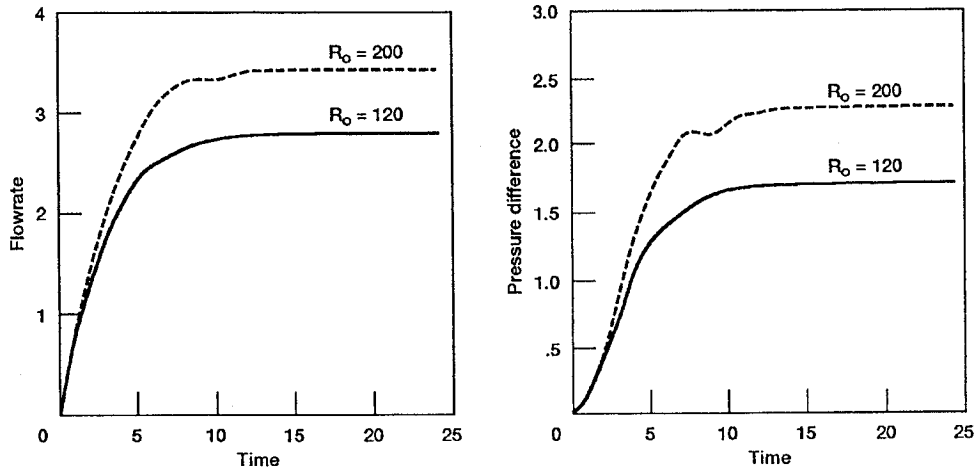

(a) Flowrate.

(b) Pressure difference.

Figure 12.—Time history of flowrate and pressure difference in a curved duct.

REPORT DOCUMENTATION PAGE

Form Approved
OMB No. 0704-0188

1. AGENCY USE ONLY (*Leave blank*)	2. REPORT DATE	3. REPORT TYPE AND DATES COVERED
	May 1992	Final Contractor Report

4. TITLE AND SUBTITLE

Direct Coupling Method for Time-Accurate Solution of Incompressible Navier-Stokes Equations

5. FUNDING NUMBERS

WU–505–62–52
C–NAS3–25266

6. AUTHOR(S)

Woo Y. Soh

7. PERFORMING ORGANIZATION NAME(S) AND ADDRESS(ES)

Sverdrup Technology, Inc.
Lewis Research Center Group
2001 Aerospace Parkway
Brook Park, Ohio 44142

8. PERFORMING ORGANIZATION REPORT NUMBER

E–7041

9. SPONSORING/MONITORING AGENCY NAMES(S) AND ADDRESS(ES)

National Aeronautics and Space Administration
Lewis Research Center
Cleveland, Ohio 44135–3191

10. SPONSORING/MONITORING AGENCY REPORT NUMBER

NASA CR–189177

11. SUPPLEMENTARY NOTES

Project Manager, James R. Scott, Internal Fluid Mechanics Division, NASA Lewis Research Center, (216) 433–5863.

12a. DISTRIBUTION/AVAILABILITY STATEMENT

Unclassified - Unlimited
Subject Category 34

12b. DISTRIBUTION CODE

13. ABSTRACT (*Maximum 200 words*)

A noniterative finite-difference numerical method is presented for the solution of the incompressible Navier-Stokes equations with second-order accuracy in time and space. Explicit treatment of convection and diffusion terms and implicit treatment of the pressure gradient give a single pressure Poisson equation when the discretized momentum and continuity equations are combined. A pressure boundary condition is not needed on solid boundaries in the staggered mesh system. The solution of the pressure Poisson equation is obtained directly by Gaussian elimination. This method is tested on flow problems in a driven cavity and a curved duct.

14. SUBJECT TERMS

Incompressible viscous flow; Pressure Poisson equation; Direct coupling; Driven cavity; Curved duct flow

15. NUMBER OF PAGES

20

16. PRICE CODE

A03

17. SECURITY CLASSIFICATION OF REPORT	18. SECURITY CLASSIFICATION OF THIS PAGE	19. SECURITY CLASSIFICATION OF ABSTRACT	20. LIMITATION OF ABSTRACT
Unclassified	Unclassified	Unclassified	